



## High-power sub-kHz linewidth lasers fully integrated on silicon

DUANNI HUANG,<sup>1,\*</sup> MINH A. TRAN,<sup>1</sup> JOEL GUO,<sup>1</sup> JONATHAN PETERS,<sup>1</sup> TIN KOMLJENOVIC,<sup>1</sup> ADITYA MALIK,<sup>1</sup> PAUL A. MORTON,<sup>2</sup> AND JOHN E. BOWERS<sup>1</sup>

<sup>1</sup>Electrical and Computer Engineering Department, University of California Santa Barbara, California 93106, USA

<sup>2</sup>Morton Photonics, 3301 Velvet Valley Dr., West Friendship, Maryland 21794, USA

\*Corresponding author: duanni@ucsb.edu

Received 28 February 2019; accepted 23 April 2019 (Doc. ID 361286); published 29 May 2019

**We demonstrate a fully integrated extended distributed Bragg reflector (DBR) laser with  $\sim 1$  kHz linewidth and over 37 mW output power, as well as a ring-assisted DBR laser with less than 500 Hz linewidth. The extended DBR lasers are fabricated by heterogeneously integrating III-V material on Si as a gain section plus a 15 mm long, low-kappa Bragg grating reflector in an ultralow-loss silicon waveguide. The low waveguide loss (0.16 dB/cm) and long Bragg grating with narrow bandwidth (2.9 GHz) are essential to reducing the laser linewidth while maintaining high output power and single-mode operation. The combination of narrow linewidth and high power enable its use in coherent communications, RF photonics, and optical sensing.** © 2019 Optical Society of America under the terms of the [OSA Open Access Publishing Agreement](#)

<https://doi.org/10.1364/OPTICA.6.000745>

### 1. INTRODUCTION

Ultralow noise (ULN) semiconductor lasers with high power are required for a wide range of applications, including high-performance coherent communications systems [1], ultraprecise timing [2], frequency synthesis [3], spectroscopy [4], and distributed sensing systems [5]. Furthermore, there is significant demand for high-power ULN lasers in RF photonic analog links and processing [6–8], as well as optically processed phase array antennas. ULN is a key requirement to any system involving optical mixing, because the noise of the laser will directly affect the fidelity of the generated RF signals. For example, two ULN lasers can be beat together in a high-speed photodetector to generate a stable microwave signal [9,10]. Another major use of ULN lasers requiring extremely low-phase noise is in the fiber optic sensing field, such as interferometric acoustic-sensing systems for exploration or sonar sensing systems or distributed sensing systems. Finally, yet another fast-growing sensing application is LiDAR, where the low-frequency-phase noise again directly impacts system performance. The common requirements for all these applications are very low relative-intensity noise (RIN) as well as very low-frequency noise and Lorentzian linewidth. Current commercial solid-state lasers [11,12] and fiber lasers [13,14] have high performance, but cannot compete with semiconductor lasers in terms of size, weight, and power (SWaP), or cost.

Recently, there has been significant interest in assembling semiconductor gain chips with long external cavities to reduce the laser linewidth. This hybrid approach is attractive because it allows for the gain chip and external cavity to be separately optimized. This starts with the material selection, and external cavities

based on planar lightwave circuits (PLC) [15], low-loss silicon nitride [16,17], and silicon [18,19] have been demonstrated. The drawback regarding these assembled hybrid semiconductor lasers is their limited scalability, because each laser must be individually assembled. Alignment between the chips is critical, which slows down the process and increases cost. Furthermore, many of the aforementioned sensing applications require the devices to be resistant to variations in pressure, shock, and vibration. This is another reason why a fully integrated solution is preferred over hybrid solutions, because the coupling between the gain chip and external cavity is sensitive to these environmental factors.

The heterogeneous silicon/III-V integration platform provides an excellent solution to this problem [20,21]. Heterogeneous integration involves the wafer bonding of unprocessed materials on a wafer-level scale, providing a clear path towards scaling and high-volume production. It benefits from mature CMOS-based silicon processing technologies and foundries. Heterogeneous integration also has the benefit of selecting the best material to perform each function (i.e., lasers, low-loss waveguides, detectors) to form highly complex photonic integrated circuits (PIC) [22]. Thus, it provides much more flexibility compared with a purely monolithic approach, while retaining the much-needed scalability that hybrid solutions lack.

This paper describes a fully integrated ULN laser, the extended distributed Bragg reflector (E-DBR) integrated laser [23], which takes advantage of the flexibility of the heterogeneous silicon platform to integrate III-V gain material along with ultralow-loss waveguides all on the same chip. Central to the design of the E-DBR is a long, low-kappa, low-loss, Bragg reflector with narrow bandwidth. This is in contrast to previous heterogeneous DBR

lasers, in which the Bragg reflector does not provide a long cavity length, and therefore does not provide much linewidth reduction [24,25]. Instead, the E-DBR follows the design philosophy of the Morton hybrid ULN laser [26,27], in which a long, custom fiber Bragg grating (FBG), is used to form the external cavity. The extended-length FBG forms the majority of the laser cavity, providing narrow laser linewidth from the long cavity, together with highly stable single-mode operation through the narrow bandwidth of the filter. First, we introduce the ultralow-loss silicon platform that enables the fabrication of a 15 mm long low- $\kappa$  grating while maintaining low loss. We discuss the layout of the E-DBR as well as a ring-assisted version (RAE-DBR), and the fabrication of these lasers. Finally, we present experimental results of the lasers, which output over 37 mW of power as well as  $\sim 1$  kHz Lorentzian linewidth.

## 2. LASER DESIGN

### A. Ultralow-Loss Silicon Platform

The key to unlocking narrow linewidth and high power is reducing waveguide loss. We have previously demonstrated ultralow loss (ULL) silicon waveguides with less than 0.16 dB/cm propagation loss across the C + L bands while maintaining single-mode operation for TE polarization. The propagation loss is further reduced to 0.04 dB/cm if multimode waveguides are considered. The geometry of the waveguide consists of a very shallow rib waveguide that is etched only 56 nm out of 500 nm. For single TE-mode operation, the width of the waveguide should be kept under 2  $\mu\text{m}$ . Further details regarding the development of this platform can be found in [28]. We compare several low-loss waveguide platforms based on foundry-compatible materials such as silicon, silicon nitride, and indium phosphide in Table 1.

Compared with other low-loss platforms, the ULL silicon platform benefits from high group index (longer effective cavity length), high power handling due to large modal volume, and ease of integration with lasers. The last point is particularly important, because the ULL silicon platform uses the same silicon thickness (500 nm) as the heterogeneous silicon/III-V laser. The 500 nm thick silicon can achieve index matching between the silicon waveguide and the III-V epitaxial stack to provide a suitable Si/III-V hybrid mode in the gain section [34–36]. The use of a thick (500 nm) silicon layer has also been demonstrated to support high linearity heterogeneous silicon/III-V modulators [37] with high operating power [38], and high bandwidth photodetectors [9].

**Table 1. Comparison of Foundry Compatible Low-loss Single-Mode Waveguide Platforms**

Platform	Optical loss per unit length [dB/cm]	Min. Bend Radius [ $\mu\text{m}$ ]	Group Index	Loss per unit time [dB/ns]
ULL SOI rib (500 nm) [28]	0.16	600	3.61	1.33
“Thin” SOI rib (220 nm) [29]	0.5	35	3.82	3.93
“Thick” SOI (>1 micron) [30]	0.027	2400	3.64	0.22
ULL Silicon Nitride [31]	0.007	10000	1.48	0.14
TriPleX Silicon Nitride [32]	0.1	100	1.7	1.76
InP [33]	0.34	11600	3.81	2.68

The seamless integration of ULL waveguides adds another component to the fast-growing heterogeneous silicon/III-V platform [22].

The requirements to fabricate a high reflectivity Bragg grating with long length and narrow bandwidth are low propagation loss and sufficiently weak perturbations, i.e., low  $\kappa$ . This is depicted in Fig. 1, in which the bandwidth and reflectivity of a uniform grating are simulated. Weakening the grating decreases the full-width half maximum (FWHM) of the grating and lowers the reflectivity. For the same  $\kappa L$ , a longer grating will provide an even narrower pass-band, but is more sensitive to the optical loss, which also decreases the reflectivity and increases mirror loss. Thus, both weak kappa and low waveguide loss are needed to achieve a narrowband grating reflector with enough reflectivity. For E-DBR lasers, we target grating strengths with  $\kappa L < 1$ , and optical losses less than 0.2 dB/cm, both of which are achievable using the ULL silicon platform.

For conventional sidewall or surface etched gratings, the power coupling coefficient  $\kappa$  is directly proportional to the perturbation in waveguide width or height, respectively. These perturbations become too small to resolve in device fabrication in the limit that  $\kappa$  approaches zero. Alternate grating designs to achieve ultralow  $\kappa$  were demonstrated for ULL  $\text{Si}_3\text{N}_4$  waveguides, including etched pillars set back from the waveguide, sampled gratings and higher order gratings [39]. This work using ULL shallow etched silicon waveguides utilizes periodically etched holes through the silicon layer on either side of the waveguide to achieve the same low  $\kappa$  values. In this design,  $\kappa$  is inversely proportional to the distance between the holes and the waveguide, which can be well controlled with lithography. The dependence between this distance and  $\kappa$  was previously simulated and experimentally verified [28]. Finally, the other component enabled by the ULL Si platform is the high-Q ring resonator, which was demonstrated to be as high as 4.1 million for intrinsic Q and 2.1 million for loaded Q. Using a high-Q ring in the laser cavity can serve to further reduce the linewidth because it provides enhanced cavity length near resonance and sharpens the cavity filter.

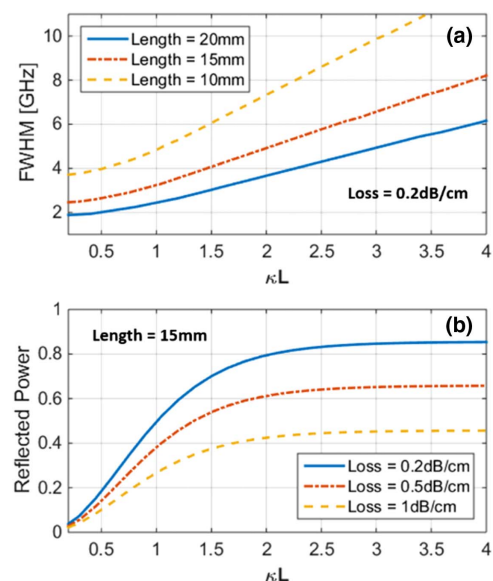


**Fig. 1.** Impact of grating strength on the (a) full-width half maximum (FWHM) bandwidth, and (b) reflected power assuming a 15 mm long uniform grating. The simulations are shown over various lengths and waveguide losses.

### B. Extended DBR Laser and Ring-Assisted Extended DBR Lasers

The two laser designs detailed in this work are shown in Fig. 2; the extended-DBR (E-DBR) laser and ring-assisted E-DBR (RAE-DBR) laser. The lasers include a tunable back mirror, a III-V on silicon gain section, a phase-control section, and a long Bragg grating-based front mirror through which the light is output. The RAE-DBR laser has an additional ring filter as part of the laser cavity to increase the effective cavity length and reduce the reflector sidelobes.

The gain section is the same for the two lasers and consists of InAlGaAs multiple quantum well (MQW) material with three quantum wells [36]. The length of the gain section is 2.5 mm, and it is connected to the ULL silicon waveguides and gratings through two tapered transitions, as shown in Fig. 2(a). Each laser also includes a phase-control section that can be tuned to align the lasing mode to the reflector peak. The tuning in the laser is achieved via thermal tuning by heating up a metallic resistor located on top of each element. There are no heaters on top of the grating, but one could be included to provide some tunability of the Bragg wavelength. The heaters are separated from the optical waveguide layers by 1 μm of sputtered oxide cladding, which is sufficient to avoid any absorption loss by the metal.

The back mirror of the lasers is a tunable reflector consisting of a Mach-Zehnder interferometer (MZI) with a loop mirror. The reflectivity of the mirror can be varied from zero to  $4s(1 - s)$ , where  $s$  is the power splitting ratio of the couplers in the MZI. To obtain the maximum tuning range,  $s$  is designed to be 0.5. A monitor photodiode (MPD) is included to monitor the reflectivity of the tunable reflector, as well as the tuning of the ring and phase sections. Finally, the light is edge coupled through a polished angled facet.

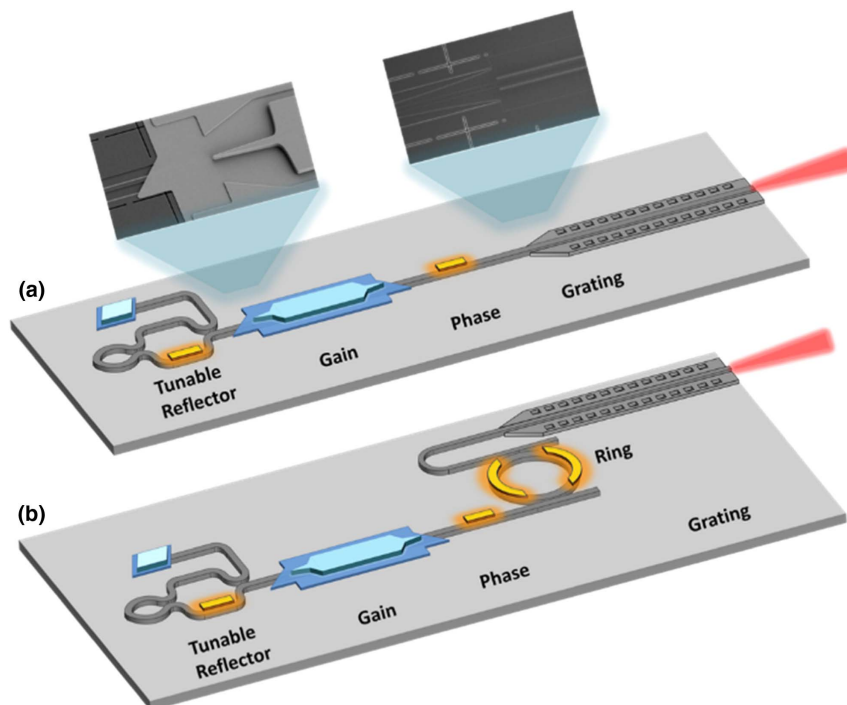


**Fig. 2.** (a) Schematic of the E-DBR laser, with SEM images of the transitions between the various sections of the laser. (b) A ring resonator is incorporated in the cavity to form the RAE-DBR laser.

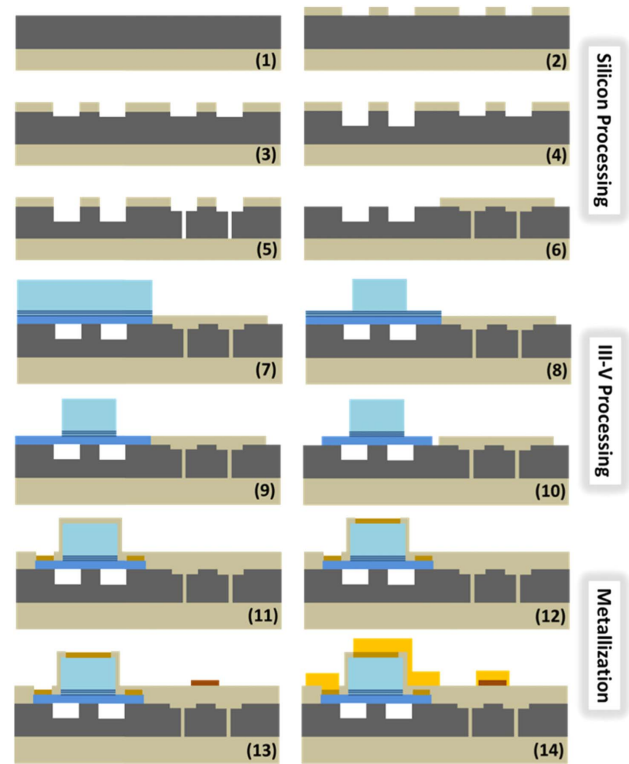


**Fig. 3.** Simplified fabrication procedure for the lasers. (1–6) The process begins with silicon processing with patterning of waveguides and gratings. (7) The III-V epi is bonded, followed by (8–10) patterning of the mesa, etching of the  $p$ -InP, MQW, and  $n$ -InP layers. The mesas are passivated, followed by (11) metallization of the  $n$ -contact, (12)  $p$ -contacts, (13) heaters, and (14) probe metal.

### 3. FABRICATION

The laser fabrication is depicted in Fig. 3. It consists of silicon patterning and etching, III-V bonding, and processing, followed by metal deposition for the contacts and heaters. The entire process is performed using a 248 nm DUV stepper for lithography, except for the gratings, which are defined using electron-beam lithography due to their small feature size (238 nm period). However, state-of-the-art lithography systems in silicon foundries can resolve these features. Otherwise, higher order gratings can also be considered [39]. The entire fabrication takes place at a wafer scale (4" SOI wafer), which demonstrates the potential scalability of the process.

Due to the multiple silicon etches with different etch depths, a SiO<sub>2</sub> hard-mask is used to define the waveguides. The etches are then carried out with the shallowest etch (56 nm) first, followed by the intermediate (231 nm) and full etch (500 nm) with photoresist masking in between each step. Because the hard-mask was used to define the waveguides during the entire process, it ensures that the transitions between waveguides with different etch depths are self-aligned and not subject to lithographic misalignment in the stepper. The ULL Si areas containing the gratings and rings are clad with SiO<sub>2</sub> to protect them from the ensuing III-V bonding and processing and preserve the low waveguide loss.

The III-V die is bonded using an O<sub>2</sub> plasma-activated direct bonding procedure, and the InP substrate is removed using a combination of lapping and wet etching. The laser mesas are etched using a series of CH<sub>4</sub>/H<sub>2</sub>/Ar dry etches as well as wet etches containing HCl or H<sub>3</sub>PO<sub>4</sub>. After the III-V processing is complete, SiO<sub>2</sub> is sputtered, and vias are opened to expose the

*n*- and *p*-contacts. The last part of the fabrication is deposition of the various metals for *n*-(Pd/Ge/Pd/Au/Ti) and *p*-contacts (Pd/Ti/Pd/Au), heaters (Pt), and probe pads (Au/Ti). The current channels are formed using proton implantation. Further details on the fabrication of heterogeneous silicon/III-V lasers can be found in Ref. [40].

### 4. RESULTS AND ANALYSIS

#### A. Reflector Characterization

The grating-based reflector for each laser is characterized by the setup shown in Fig. 4(a). The gain section of the laser is reverse biased to operate as a photodiode, and the photocurrent is recorded as light from an external tunable laser is injected through the grating.

For the E-DBR, the photocurrent provides a direct measurement of the transmission spectrum through the grating. The reflection spectrum can then be calculated from the measurement. This method directly characterizes the reflector in the laser rather than relying on test structures, which could deviate from the actual grating in the laser. This also largely avoids the influence of Fabry–Perot ripples from reflections off facets and fibers, which often corrupt the measurement if the reflection spectrum of the grating is measured directly with the use of a circulator. The results for three 15 mm long grating reflectors with designed  $\kappa L = 0.375, 0.75, \text{ and } 3$  are shown in Fig. 4(b). As the grating strength increases, the bandwidth and reflectivity increase as well. For the weakest grating, the 3-dB bandwidth of the grating is 2.9 GHz, and the peak reflectivity is roughly 40%.

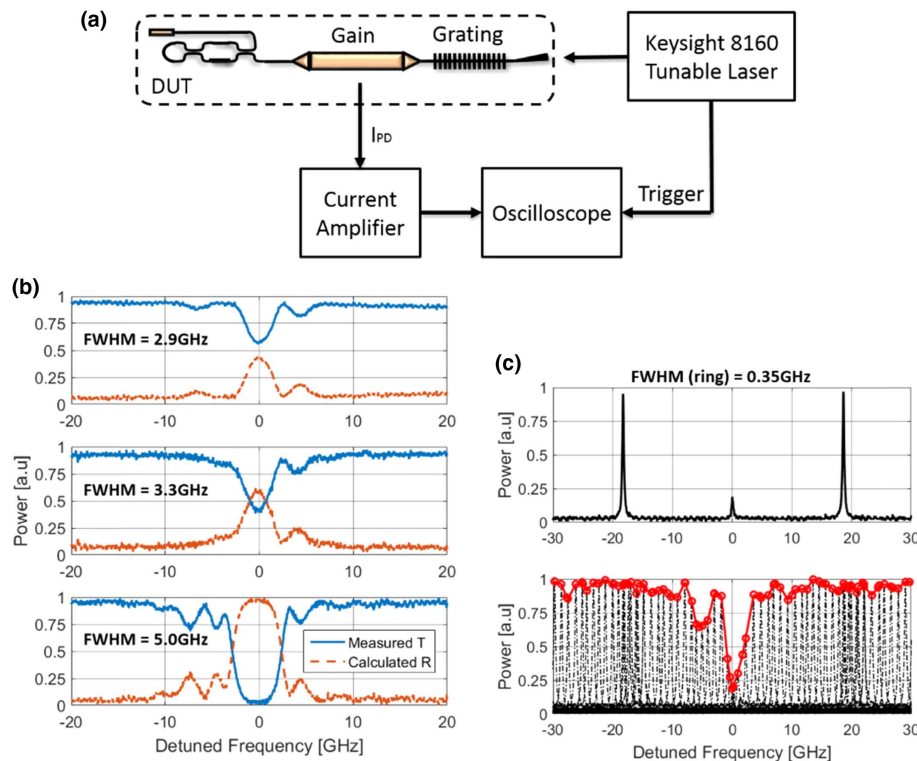


**Fig. 4.** (a) Test setup used to characterize the grating-based reflectors in each laser without having to use separate test structures. (b) The measurements for the E-DBR are shown for a 15 mm long grating with designed  $\kappa L = 0.375, 0.75, \text{ and } 3$ , respectively. (c) The measurement for the RAE-DBR is shown, in which the transmission through both the grating and ring is recorded. By tuning the ring across a full FSR, the shape of the grating can be revealed.

For the RAE-DBR, the photocurrent is a measurement of the grating transmission multiplied by the transmission of the ring filter, as seen from the drop-port. The resulting measurement is shown in Fig. 4(c), in which the ring resonance at the Bragg wavelength is suppressed by the stopband of the grating. The FWHM of the ring is only 0.35 GHz, which is over 10 times narrower than the grating. To map out the response of the grating, we tune the ring across a full FSR (18.5 GHz) while recording the photocurrent. The resulting traces are overlaid on top of each other in Fig. 4(c), in which the transmission through the grating is viewed. The FWHM of the grating is roughly 4 GHz, which is much smaller than the FSR of the ring. Thus, only the resonance at the Bragg wavelength will provide reflection back into the laser. The peak reflectivity of the grating is estimated to be nearly 80%, which is higher than expected, given the designed  $\kappa L = 1$ .

**B. Laser Characterization**

The lasers are characterized on a temperature-controlled stage at room temperature. The output power is measured with a broad-area photodetector, as well as a lensed fiber. Comparisons between the two show 6.5 dB of coupling loss from the 8-deg angled facet to the lensed fiber, which agrees with simulations. This can be reduced with the use of a spot-size converter on the laser output. The tunable loop mirror is set to provide maximum reflection by minimizing the photocurrent at the monitor photodiode, providing the condition with the lowest threshold current for the laser.

The measured LIV curve for an E-DBR laser with a designed  $\kappa L = 0.375$  is shown in Fig. 5(a). The laser has a threshold current of 50 mA and a maximum on-chip power of over 37 mW. When coupled into a fiber, the maximum power in the fiber is

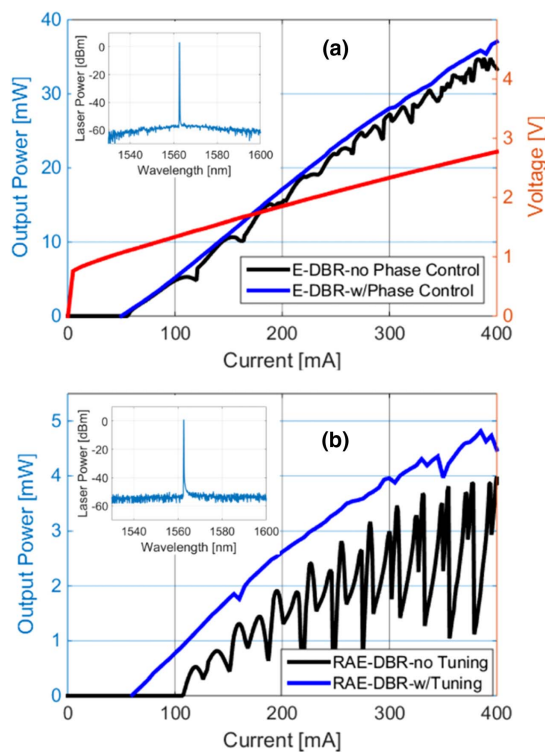


**Fig. 5.** (a) LIV curve for the E-DBR laser with  $\kappa L = 0.375$  with and without active tuning of the phase control section. The on-chip output power reaches over 37 mW. (b) The LI characteristics of the RAE-DBR are shown with and without active tuning of the ring heater.

8.3 mW. Kinks in the laser power correspond to longitudinal mode hopping in the E-DBR caused by heating of the gain section as the current is increased. This causes the lasing mode to be detuned from the grating peak, which reduces the output power until eventually, the lasing mode hops to the next longitudinal mode. These mode hops are more common at higher currents, because Joule heating is more significant at high currents. By controlling the laser cavity phase, with the tunable phase control element, the E-DBR lasing mode can be aligned with the grating peak through a large part of the LIV curve, providing the cleaner and continuous single-mode output blue curve shown in Fig. 5(a). A spectrum of the E-DBR laser is included in the inset, for which the side-mode suppression ratio (SMSR) is over 55 dB.

The LIV of a RAE-DBR laser is shown in Fig. 5(b), shown both with and without tuning of the ring. Because the FWHM of the ring is smaller than the grating, it must be tuned to the Bragg wavelength to minimize losses—providing the higher power and cleaner blue curve. We observe a threshold current of 60 mA and on-chip maximum output power of 4.8 mW. The output power of the RAE-DBR is much lower than the E-DBR due to the higher cavity losses (both propagation loss and coupling loss) going through the add-drop ring twice per round trip, as well as a higher output mirror loss due to stronger than designed grating reflectivity. These losses can be reduced by weakening the grating, increasing the ring coupling coefficients, and/or moving the ring to the back mirror (inside the tunable reflector) so that the light only undergoes one path through

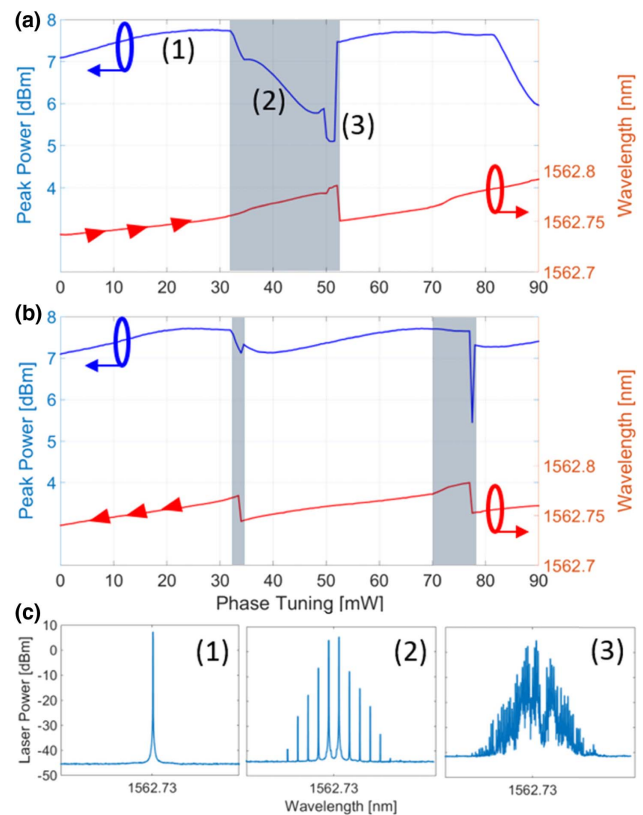


**Fig. 6.** At a fixed gain of 200 DBR mA, the laser encounters different multimode regimes, which are shaded, depending on whether the longitudinal modes are (a) red shifted with increasing power to the phase section, or (b) blue shifted. In (c) the multimode regions, the laser can enter (2) a mode-locked state or (3) a chaotic state.

the ring per round trip in the cavity. The SMSR for the RAE-DBR laser is also over 55 dB.

Operating the E-DBR near a mode hop can result in multimode, chaotic, or self-pulsing behavior [41,42]. To study these mode hops in more detail, the power to the phase control section was tuned (up and down) at a fixed gain current of 200 mA, while monitoring the

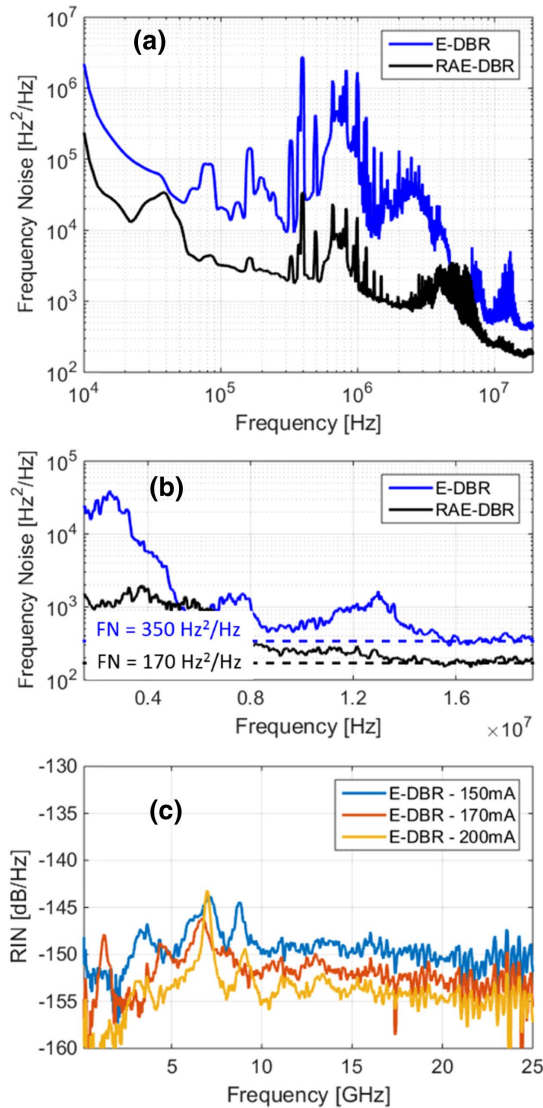


**Fig. 7.** Frequency noise spectra for the E-DBR and RAE-DBR lasers on (a) logarithmic and (b) linear frequency scales. The analyzer is limited to 20 MHz, which may not be sufficient to see the white noise floor of the FN. (c) RIN measurements of the E-DBR with  $\kappa L = 0.375$  at different drive currents.

lasing wavelength and peak power at that wavelength using a Yokogawa AQ6150 wave meter. The results are shown in Fig. 6. When the laser operates in the vicinity of a mode hop, there is a sudden drop in output power at the lasing wavelength, as multiple longitudinal modes compete to lase. High resolution scans with an OSA show that the E-DBR undergoes several transitions. The laser displays hysteresis effects as to where these mode hops happen. It also appears to be more stable when decreasing the phase power, which shifts the longitudinal modes to shorter wavelengths, than when increasing the phase power. This may be due to the slightly asymmetric spectral response of the grating, as was previously shown in Fig. 4. The on-chip MPD provides an excellent tool for providing real-time feedback as to whether the laser is approaching a mode-hop region, signaling that the phase should be tuned. The mode hops are avoided by actively tuning the phase section along with the gain—as shown in the blue LI curve in Fig. 5(a).

**C. Spectral Linewidth and RIN**

The frequency noise (FN) of the lasers is measured using a Sycatus A0040A optical noise analyzer and Keysight X-series signal analyzer. The intrinsic linewidth, or Lorentzian linewidth of the laser can then be extracted by analyzing the FN at higher frequencies where the measurement is relatively free from technical noise from electronics, vibrations, and other environmental factors. Despite using battery powered current sources isolated from power lines, there is still significant contribution to the FN from other sources in the 10 kHz to 10 MHz range. Packaging the laser and reducing the number of exposed electrical probes may alleviate these noise sources.

Furthermore, within the 20 MHz limit of the tool’s measurable frequency range, the white-noise limited frequency noise has not fully reached its flat level (i.e., the fundamental/Lorentzian linewidth). The spectra shown in Figs. 7(a) and 7(b) indicate white-noise limited frequency noise of lower than 350 Hz<sup>2</sup>/Hz for the E-DBR laser, and lower than 170 Hz<sup>2</sup>/Hz for the RAE-DBR laser, corresponding to less than 1.1 kHz and 500 Hz Lorentzian linewidths after multiplying by  $\pi$ . A comparison of E-DBR lasers with different grating strengths is shown in Table 2. The correlation between grating strength and linewidth and optical power is clear for the E-DBR. The grating strength does not play a large role in determining the RAE-DBR’s linewidth, as expected due to the ring being much more narrowband than the grating. A straightforward improvement is to decrease the grating strength for the RAE-DBR, which would lead to higher output power.

The relative intensity noise (RIN) spectra measured for the E-DBR laser at several drive currents are shown in Fig. 7(c). There are several peaks in the 0–10 GHz range, which are attributed to mode interactions between the lasing mode and nonlasing cavity modes. This may be further suppressed by optimizing the

**Table 2. Comparison of Lorentzian Linewidth of E-DBR and RAE-DBR**

Laser Type	Grating Length [mm]	Designed $\kappa L$	Ring Power Coupling	Ring Radius [ $\mu\text{m}$ ]	Power at 400 mA [mW]	Linewidth [kHz]
E-DBR	15	0.375	—	—	37	1.1
E-DBR	15	0.75	—	—	18	1.5
E-DBR	15	1.05	—	—	12	4.0
E-DBR	15	3	—	—	3.1	10.0
RAE-DBR	10	1	0.04	600	4.8	0.5
RAE-DBR	10	2	0.04	600	2.1	0.6

phase control at each drive current, as was demonstrated in the LIV. Grating apodization could suppress these peaks by improving the SMSR. For 200 mA drive current, the RIN is measured to be less than  $-150$  dB/Hz apart from the dominant peak at 7 GHz.

## 5. CONCLUSIONS

We demonstrate heterogeneously integrated E-DBR lasers on silicon with  $\sim 1$  kHz linewidth and over 37 mW of output power. Adding a high-Q ring into the cavity further reduces the linewidth to 500 Hz, however, with a lower output power of 4.8 mW. The narrow linewidth and excellent single-mode stability are achieved by using ultralow-loss silicon waveguides with extremely low kappa gratings to form a 15 mm long extended Bragg reflector. Future work includes grating apodization to increase SMSR and reduce multimode effects, as well as improved design of the ring in the RAE-DBR to minimize losses.

**Funding.** Defense Advanced Research Projects Agency (DARPA) (HR0011-15-C-055, W911NF-19-C-0003).

**Acknowledgment.** The views and conclusions in this paper are those of the authors and should not be interpreted as presenting the official policies or position, either expressed or implied, of DARPA or the U.S. Government. The U.S. Government is authorized to reproduce and distribute reprints for Government purposes notwithstanding any copyright notation hereon. We also acknowledge Sycatus/Keysight and Ogmentum for the loan of frequency noise-measurement equipment.

## REFERENCES

- S. L. I. Olsson, J. Cho, S. Chandrasekhar, X. Chen, P. J. Winzer, and S. Mavejjs, "Probabilistically shaped PDM 4096-QAM transmission over up to 200 km of fiber using standard intradyne detection," *Opt. Express* **26**, 4522–4530 (2018).
- Z. L. Newman, V. Maurice, T. E. Drake, J. R. Stone, T. C. Briles, D. T. Spencer, C. Fredrick, Q. Li, D. Westly, B. R. Ilic, B. Shen, M.-G. Suh, K. Y. Yang, C. Johnson, D. M. S. Johnson, L. Hollberg, K. Vahala, K. Srinivasan, S. A. Diddams, J. Kitching, S. B. Papp, and M. T. Hummon, "Photonic integration of an optical atomic clock," arXiv:1811.00616 (2018).
- D. T. Spencer, T. Drake, T. C. Briles, J. Stone, L. C. Sinclair, C. Fredrick, Q. Li, D. Westly, B. R. Ilic, A. Bluestone, N. Volet, T. Komljenovic, L. Chang, S. H. Lee, D. Y. Oh, T. J. Kippenberg, E. Norberg, L. Theogarajan, M. Suh, K. Y. Yang, H. P. Martin, K. Vahala, N. R. Newbury, K. Srinivasan, J. E. Bowers, S. A. Diddams, and S. B. Papp, "An optical-frequency synthesizer using integrated photonics," *Nature* **557**, 81–85 (2018).
- M. G. Suh, Q. F. Yang, K. Y. Yang, X. Yi, and K. J. Vahala, "Microresonator soliton dual-comb spectroscopy," *Science* **354**, 600–603 (2016).
- J. Geng, C. Spiegelberg, S. Jiang, and A. Abstract, "Narrow linewidth fiber laser for 100-km optical frequency domain reflectometry," *IEEE Photon. Technol. Lett.* **17**, 1827–1829 (2005).
- C. Middleton, S. Meredith, R. Peach, and R. Desalvo, "Photonic frequency conversion for wideband RF-to-IF down-conversion and digitization," in *IEEE Avionics, Fiber-Optics and Photonics Technology Conference* (2011), pp. 115–116.
- D. Marpaung, C. Roeloffzen, R. G. Heideman, A. Leinse, S. Sales, and J. Campamy, "Integrated microwave photonics," *Laser Photon. Rev.* **7**, 506–538 (2013).
- P. A. Morton and Z. Mizrahi, "Low-cost, low-noise hybrid lasers for high SFDR RF photonic links," in *IEEE Avionics, Fiber-Optics and Photonics Digest CD* (2012), pp. 64–65.
- J. Hulme, M. Kennedy, R.-L. Chao, L. Liang, T. Komljenovic, J.-W. Shi, B. Szafraniec, D. Baney, and J. E. Bowers, "Fully integrated microwave frequency synthesizer on heterogeneous silicon-III/V," *Opt. Express* **25**, 2422–2431 (2017).
- J. Yao, "Microwave photonics: photonic generation of microwave and millimeter-wave signals," *Int. J. Microw. Opt. Technol.* **5**, 16–21 (2010).
- T. J. Kane and R. L. Byer, "Monolithic, unidirectional single-mode Nd:YAG ring laser," *Opt. Lett.* **10**, 65–67 (1985).
- "Continuous Wave Single Frequency IR Laser NPRO 125/126 Series," <https://www.lumentum.com/en/products/laser-solid-state-cw-1064-1319-npro>.
- "NP Photonics," <http://www.npphotonics.com/rock-module>.
- "Koheras Adjustik E15," <https://www.nktphotonics.com/wp-content/uploads/sites/3/2015/04/koheras-adjustik-e15.pdf?1550069496>.
- A. Verdier, G. De Valicourt, R. Brenot, H. Debregeas, H. Carr, and Y. Chen, "Ultrawideband wavelength-tunable hybrid external-cavity lasers," *J. Lightwave Technol.* **36**, 37–43 (2018).
- B. Stern, X. Ji, A. Dutt, and M. Lipson, "Compact narrow-linewidth integrated laser based on a low-loss silicon nitride ring resonator," *Opt. Lett.* **42**, 4541–4544 (2017).
- Y. Fan, R. M. Oldenbeuving, C. G. Roeloffzen, M. Hoekman, D. Geskus, R. G. Heideman, and K. Boller, "290 Hz intrinsic linewidth from an integrated optical chip-based widely tunable InP-Si<sub>3</sub>N<sub>4</sub> hybrid laser," in *Conference on Lasers and Electro-Optics* (2017), paper JTh5C.9.
- H. Guan, A. Novack, T. Galfsky, Y. Ma, S. Fatholouloumi, A. Horth, T. N. Huynh, J. Roman, R. Shi, M. Caverley, Y. Liu, T. Baehr-Jones, K. Bergman, and M. Hochberg, "Widely-tunable, narrow-linewidth III-V/silicon hybrid external-cavity laser for coherent communication," *Opt. Express* **26**, 7920–7933 (2018).
- N. Kobayashi, K. Sato, M. Namiwaka, K. Yamamoto, S. Watanabe, T. Kita, H. Yamada, and H. Yamazaki, "Silicon photonic hybrid ring-filter external cavity wavelength tunable lasers," *J. Lightwave Technol.* **33**, 1241–1246 (2015).
- A. W. Fang, H. Park, O. Cohen, R. Jones, M. J. Paniccia, and J. E. Bowers, "Electrically pumped hybrid AlGaInAs-silicon evanescent laser," *Opt. Express* **14**, 9203–9210 (2006).
- T. Komljenovic, M. Davenport, J. Hulme, A. Liu, C. Santis, A. Spott, S. Srinivasan, E. Stanton, C. Zhang, and J. Bowers, "Heterogeneous silicon photonic integrated circuits," *J. Lightwave Technol.* **34**, 20–35 (2015).
- T. Komljenovic, D. Huang, P. Pintus, M. A. Tran, M. L. Davenport, and J. E. Bowers, "Photonic integrated circuits using heterogeneous integration on silicon," *Proc. IEEE* **106**, 2246–2257 (2018).
- D. Huang, M. A. Tran, J. Guo, J. Peters, T. Komljenovic, A. Malik, P. Morton, and J. E. Bowers, "Sub-kHz linewidth extended-DBR lasers heterogeneously integrated on silicon," in *2019 Optical Fiber Communications Conference and Exhibit (OFC)*, San Diego, California, USA, 3–7 March 2019.
- S. Keyvaninia, G. Roelkens, D. Van Thourhout, C. Jany, M. Lamponi, A. Le Liepvre, F. Lelarge, D. Make, G.-H. Duan, D. Bordel, and J.-M. Fedeli, "Demonstration of a heterogeneously integrated III-V/SOI single wavelength tunable laser," *Opt. Express* **21**, 3784–3792 (2013).
- A. W. Fang, B. R. Koch, R. Jones, E. Lively, D. Liang, Y. H. Kuo, and J. E. Bowers, "A distributed Bragg reflector silicon evanescent laser," *IEEE Photon. Technol. Lett.* **20**, 1667–1669 (2008).
- P. A. Morton, "Ultra-low noise, highly stable single-mode operation, high power, Bragg grating based semiconductor laser," U.S. patent 10/193,306 (22 February 2018).
- P. A. Morton and M. J. Morton, "High-power, ultra-low noise hybrid lasers for microwave photonics and optical sensing," *J. Lightwave Technol.* **36**, 5048–5057 (2018).
- M. Tran, D. Huang, T. Komljenovic, J. Peters, A. Malik, and J. Bowers, "Ultra-low-loss silicon waveguides for heterogeneously integrated silicon/III-V photonics," *Appl. Sci.* **8**, 1139 (2018).
- P. P. Absil, P. De Heyn, H. Chen, P. Verheyen, G. Lepage, M. Pantouvaki, J. De Coster, A. Khanna, Y. Drissi, D. Van Thourhout, and J. Van Campenhout, "Imec iSiPP25G silicon photonics: a robust CMOS-based photonics technology platform," *Proc. SPIE* **9367**, 93670V (2015).
- A. Biberman, M. J. Shaw, E. Timurdogan, J. B. Wright, and M. R. Watts, "Ultralow-loss silicon ring resonators," *Opt. Lett.* **37**, 4236–4241 (2012).
- D. Dai, J. Bauters, and J. E. Bowers, "Passive technologies for future large-scale photonic integrated circuits on silicon: polarization handling, light non-reciprocity and loss reduction," *Light: Sci. Appl.* **1**, e1 (2012).
- C. G. H. Roeloffzen, M. Hoekman, E. J. Klein, L. S. Wevers, R. B. Timens, D. Marchenko, D. Geskus, R. Dekker, A. Alippi, R. Grootjans,

- A. Van Rees, R. M. Oldenbeuving, J. P. Epping, R. G. Heideman, K. Worhoff, A. Leinse, D. Geuzebroek, E. Schreuder, P. W. L. Van Dijk, I. Visscher, C. Taddei, Y. Fan, C. Taballione, Y. Liu, D. Marpaung, L. Zhuang, M. Benelajla, and K. J. Boller, "Low-loss Si<sub>3</sub>N<sub>4</sub> triplex optical waveguides: technology and applications overview," *IEEE J. Sel. Top. Quantum Electron.* **24**, 1–21 (2018).
33. D. D'Agostino, G. Carnicella, C. Ciminelli, P. Thijs, P. J. Veldhoven, H. Ambrosius, and M. Smit, "Low-loss passive waveguides in a generic InP foundry process via local diffusion of zinc," *Opt. Express* **23**, 25143–25157 (2015).
34. D. X. Xu, J. H. Schmid, G. T. Reed, G. Z. Mashanovich, D. J. Thomson, M. Nedeljkovic, X. Chen, D. Van Thourhout, S. Keyvaninia, and S. K. Selvaraja, "Silicon photonic integration platform-have we found the sweet spot?" *IEEE J. Sel. Top. Quantum Electron.* **20**, 8100217 (2014).
35. A. Yariv and X. Sun, "Supermode Si/III-V hybrid lasers, optical amplifiers and modulators: a proposal and analysis," *Opt. Express* **15**, 9147–9151 (2007).
36. M. L. Davenport, S. Skendzic, N. Volet, J. C. Hulme, M. J. R. Heck, and J. E. Bowers, "Heterogeneous silicon/III-V semiconductor optical amplifiers," *IEEE J. Sel. Top. Quantum Electron.* **22**, 78–88 (2016).
37. C. Zhang, P. A. Morton, J. B. Khurgin, J. D. Peters, and J. E. Bowers, "Ultralinear heterogeneously integrated ring-assisted Mach-Zehnder interferometer modulator on silicon," *Optica* **3**, 1483–1488 (2016).
38. P. A. Morton, M. J. Morton, C. Zhang, J. B. Khurgin, J. Peters, C. D. Morton, and J. E. Bowers, "High-power, high-linearity, heterogeneously integrated III-V on Si MZI modulators for RF photonics systems," *IEEE Photon. J.* **11**, 5501310 (2019).
39. D. T. Spencer, M. Davenport, S. Srinivasan, J. Khurgin, P. A. Morton, and J. E. Bowers, "Low kappa, narrow bandwidth Si<sub>3</sub>N<sub>4</sub> Bragg gratings," *Opt. Express* **23**, 30329–30336 (2015).
40. M. Davenport, "Heterogeneous silicon III-V mode-locked lasers," Ph.D. dissertation (University of California, Santa Barbara, 2017).
41. P. Bardella and I. Montrosset, "Analysis of self-pulsating three-section DBR lasers," *IEEE J. Sel. Top. Quantum Electron.* **11**, 361–366 (2005).
42. X. Pan, H. Olesen, and B. Tromborg, "A theoretical model of multielectrode DBR lasers," *IEEE J. Quantum Electron.* **24**, 2423–2432 (1988).